

Molecular formations and spectra due to electron correlations in three-electron hybrid double-well qubits

Constantine Yannouleas^{✉*} and Uzi Landman^{✉†}*School of Physics, Georgia Institute of Technology, Atlanta, Georgia 30332-0430, USA*
 (Received 22 December 2021; revised 18 April 2022; accepted 19 April 2022; published 3 May 2022)

We show that systematic full configuration-interaction (FCI) calculations enable prediction of the energy spectra and the intrinsic spatial and spin structures of the many-body wave functions as a function of the detuning parameter for the case of three-electron hybrid qubits based on GaAs asymmetric double quantum dots. Specifically, in comparison with the case of weak interactions and treating the entire three-electron double-dot hybrid qubit as an integral unit, it is shown that the predicted spectroscopic patterns, originating from strong electron correlations, manifest the formation of Wigner molecules (WMs). Signatures of WM formation include: (1) a strong suppression of the energy gaps relative to the noninteracting-electron modeling, and (2) the appearance of a pair of avoided crossings arising between states associated with two-electron occupancies in the left and right wells. The Wigner molecule is a physical entity associated with electron localization within each well, and it cannot be captured by the previously employed independent-particle or two-site-Hubbard theoretical modeling of the hybrid qubits. The emergence of strong WMs is investigated in depth through the concerted use of FCI-adapted diagnostic tools like charge and spin densities, as well as conditional probability distributions. Furthermore, the energy spectrum as a function of the strength of the Coulomb repulsion (at constant detuning) is calculated in order to complement the thorough analysis of the factors contributing to WM emergence. We report remarkable agreement with recent experimental measurements. The present FCI methodology for multiwell quantum dots can be straightforwardly extended to treat valleytronic two-band Si/SiGe hybrid qubits, where the central role of the WMs was confirmed recently. Such valleytronic FCI could be also adapted and employed in simulations of Si-based two-qubit logical gates made of two interacting double-quantum-dot hybrid qubits confining a total of $N \leq 6$ electrons.

DOI: [10.1103/PhysRevB.105.205302](https://doi.org/10.1103/PhysRevB.105.205302)

I. INTRODUCTION

Methodical control of the parameters and performance of qubits is a prerequisite for the successful implementation of quantum computing. To this effect, during the last decade major experimental endeavors (see, e.g., Refs. [1–7]) have been undertaken and substantial progress has been reported. In particular, unprecedented progress has been achieved in the techniques for controlling and manipulating the spin and charge electronic degrees of freedom of two-dimensional (2D) semiconductor hybrid-double-quantum-dot (HDQD) qubits [8–15], comprising three-electron (3e) [8–10,12,13,15] and five-electron (5e) [11,14] varieties.

Nonetheless, several experimental scrutinies in the last two years of state-of-the-art semiconductor double-dot Si/SiGe [14] and GaAs [15] HDQD qubit devices have provided incontrovertible evidence (see also Refs. [16,17]) that a key factor influencing the qubit spectra and performance had been overlooked in the context of earlier qubit investigations. This factor is the manifestation of strong electron-electron (e-e) correlations leading to formation of Wigner molecules (WMs) [18–31], which rearranges sharply the electronic spectra of the qubit device with respect to

those associated with noninteracting electrons. As their name suggests, the WMs are a fully quantal extension of the concept of a bulk Wigner crystal [32] to the realm of finite systems.

From a theoretical perspective, the formation of Wigner molecules cannot be described in the framework of independent-particle (single-particle) modeling [8,33,34], which was advanced for 2D quantum dots (QDs) from the very early stages of the field [35], nor are the more involved *two-site* Hubbard models [8,36–41] adequate in this respect [42]. As reaffirmed recently for the case of two particles (two electrons [14–17] or two holes [17]) in a single QD, explored in recent experimental investigations [14,15], formation of WMs, which has been extensively demonstrated in earlier investigations [18,20,21,23,27–30,43,44], requires the employment of more comprehensive, *ab-initio*-in-nature, theoretical approaches, including the symmetry-breaking/symmetry-restoration [18,20,23,29] methods and the full configuration-interaction (FCI) method (referred to also as exact diagonalization [21,27–30,43–46]).

In this paper we demonstrate the central role that strong e-e correlations and WM formation play in shaping the spectra of semiconductor qubits by going beyond the aforementioned recent two-particle CI calculations in a single dot [14–17], namely, we present FCI calculations for the case of a hybrid [8–15,33] *three-electron* double-quantum-dot GaAs qubit, treated as an integral unit. To establish contact

*Constantine.Yannouleas@physics.gatech.edu

†Uzi.Landman@physics.gatech.edu

with an actual experimental investigation, we employ HDQD parameters comparable to those in Ref. [15], which measured the energy spectrum of the qubit as a function of the detuning at zero magnetic field. As we elaborate below, we find a remarkable agreement between our 3e-CI energy spectra and the essential experimental trends that characterize the hybrid qubit. These trends include the large suppression of the energy gaps compared to the simple noninteracting-electron problem and the emergence of the phenomenological 4×4 effective Hamiltonian, which incorporates a pair of avoided crossings associated with double electronic occupancies in the left and right well, and which depends linearly on the detuning between the two wells.

We further present a detailed analysis of the interplay of the spectral features of the HDQD and the formation of a WM, by investigating charge and spin-resolved densities, as well as spin-resolved conditional probability distributions (CPDs), for the six or eight lowest-in-energy states of the 3e double-quantum-dot (DQD) spectra for two different cases, namely, as a function of detuning (keeping constant the dielectric constant κ) and as a function of the dielectric constant (keeping the detuning constant). In this context, particularly revealing for the process of WM formation is the contrast of charge densities (see Fig. 1 below) between a weakly interacting case (with $\kappa = 1000$) and the strongly interacting case (with $\kappa = 12.5$) of the GaAs HDQD qubit.

Plan of the paper. In Sec. II we introduce the many-body Hamiltonian of the HDQD device model, comprising three electrons in an asymmetric 2D double-well external confinement, which is modeled by a two-center-oscillator (TCO) potential joined by a smooth neck. The values of the model's parameters, employed in the calculations, are specified in this section; they are chosen to address the experiments on GaAs HDQD in Ref. [15]. Also included (Sec. II A) in this section is a restatement of the Wigner parameter R_W [18,29] pertaining to the propensity for Wigner-molecule formation, as well as estimates of the R_W corresponding to the parameters used in our calculations.

In Sec. III, the CI-calculated energy spectra as a function of the interdot detuning parameter at specific values of the dielectric constant (controlling the strength of the Coulomb repulsion) are discussed (Sec. III A) for both the case where the interelectron interaction is taken to be small (simulating the independent-electron limit) and for the actual value appropriate for GaAs (illustrating the effect of strong WM formation on the eigenvalue spectra). Subsequently (Secs. III A 1 and III A 2), we analyze the charge densities and spin structures corresponding to selected values of the detuning parameter away from the avoided crossings using both spin-resolved charge densities and spin-resolved CPDs. Special attention is devoted in Sec. III B to the evolution of the spectral characteristics and the mixing of WM wave functions (Sec. III B 1) when the detuning values fall in the neighborhood of the avoided crossings. In Sec. III C we focus on the energy gap between the ground and first excited state, and report remarkable agreement with the measurements of Ref. [15]. We end Sec. III with an analysis (Sec. III D) of the CI-calculated spectra for GaAs in the context of a phenomenological matrix Hamiltonian used as a diagnostic tool in previous works on HDQD qubits.

The effects of interelectron interaction on the Wigner-molecule formation and associated spectral characteristics are further highlighted and accentuated in Sec. IV through the analysis of the CI-calculated spectra and charge densities as a function of the dielectric constant of the material at a constant detuning value. We summarize our results in Sec. V.

Appendix A describes the numerical approach to determine the eigenenergies and eigenstates of the one-body TCO Hamiltonian introduced below in Eq. (3). Because the community of quantum-information and quantum-computer scientists have only recently become alerted [14–17] to the potentialities of the CI many-body method and the significance of the concept of the Wigner molecule, for completeness and pedagogical reasons, we include two additional Appendices as follows: Appendix B describes the CI methodology, whereas Appendix C describes the diagnostic tools (beyond-mean-field single-particle densities and CPDs, and their spin-resolved varieties) needed to analyze the CI many-body wave functions and extract the information regarding WM formation and the intrinsic spin structure of the associated CI wave function.

II. MANY-BODY HAMILTONIAN AND PARAMETERS OF THE DOUBLE-WELL DEVICE

Following the recent advances [11,13–15] in the fabrication of hybrid qubits, we investigate in this paper the many-body spectra and wave functions of three electrons in an asymmetric two-dimensional double-well external confinement, implemented by a TCO potential as described below.

We consider a many-body Hamiltonian for N electrons of the form

$$\mathcal{H}_{\text{MB}}(\mathbf{r}_i, \mathbf{r}_j) = \sum_{i=1}^N H_{\text{TCO}}(i) + \sum_{i=1}^N \sum_{j>i}^N V(\mathbf{r}_i, \mathbf{r}_j), \quad (1)$$

where $\mathbf{r}_i, \mathbf{r}_j$ denote the vector positions of the i and j electron. This Hamiltonian is the sum of a single-particle part $H_{\text{TCO}}(i)$, which implements the double-well confinement, and the two-particle interaction $V(\mathbf{r}_i, \mathbf{r}_j)$. A notable property of H_{TCO} is the fact that it allows for the formation of a smooth interwell barrier between the individual wells; see the inset of Fig. 1(b) for an illustration.

Naturally, for the case of electrons, the two-body interaction is given by the Coulomb repulsion

$$V(\mathbf{r}_i, \mathbf{r}_j) = \frac{e^2}{\kappa |\mathbf{r}_i - \mathbf{r}_j|}, \quad (2)$$

where κ is the dielectric constant of the semiconductor material.

In the two-dimensional TCO employed by us, the single-particle levels associated with the confining potential are determined by the single-particle Hamiltonian [18,23,44]

$$H_{\text{TCO}} = \frac{\mathbf{p}^2}{2m^*} + \frac{1}{2}m^*\omega_y^2 y^2 + \frac{1}{2}m^*\omega_{xk}^2 x_k'^2 + V_{\text{neck}}(x) + h_k, \quad (3)$$

where $x_k' = x - x_k$ with $k = 1$ for $x < 0$ (left) and $k = 2$ for $x > 0$ (right), and the h_k 's control the relative depth of the two wells, with the detuning defined as $\varepsilon = h_1 - h_2$. y denotes the coordinate perpendicular to the interdot axis (x). The most

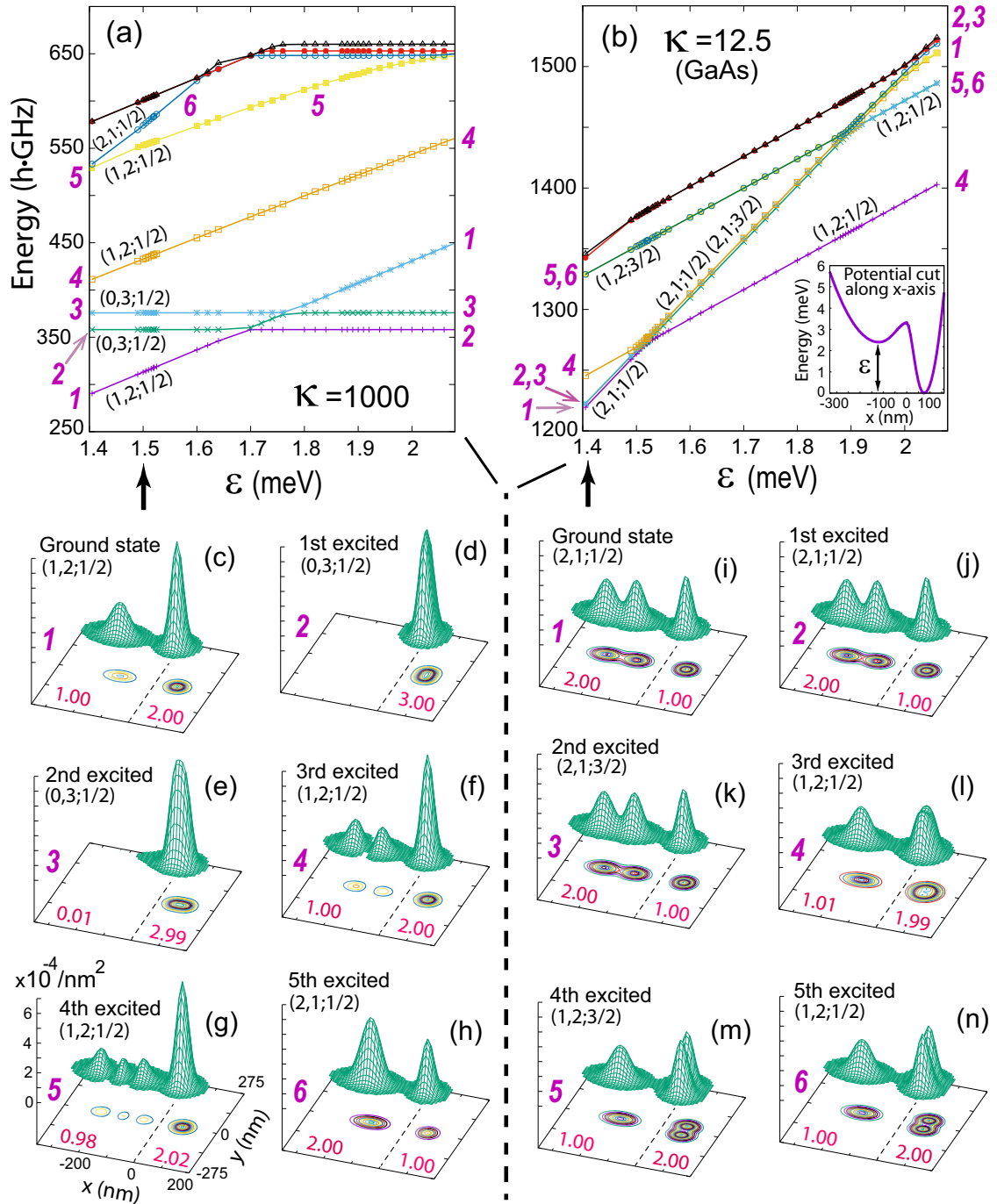


FIG. 1. Spectra for the same three-electron double dot for two different values of the dielectric constant. (a) $\kappa = 1000$ (weak Coulombic repulsion). (b) $\kappa = 12.5$ (actual value for GaAs, stronger Coulombic repulsion). (c–h) Charge densities for the ground and first five excited states for $\kappa = 1000$. (i–n) Charge densities for the ground and first five excited states for $\kappa = 12.50$. The arrows indicate the value of the detuning at which the charge densities were calculated, i.e., $\epsilon = 1.50$ meV for (c–h) and $\epsilon = 1.405$ for (i–n). The notation $(n_L, n_R; S)$ denotes the left electron occupation, the right electron occupation, and the total spin, respectively. For all densities, the scales of all three axes are as in (g). CI left and right occupations are highlighted in red. In all figures and in the text, the CI energies have been referenced to $3\hbar\sqrt{(\omega_{x_1}^2 + \omega_y^2)/2}$.

general shapes described by H are two semiellipses connected by a smooth neck $[V_{\text{neck}}(x)]$. $x_1 < 0$ and $x_2 > 0$ are the centers of these semiellipses, $d = x_2 - x_1$ is the interdot distance, and m^* is the effective electron mass.

For the smooth neck we use

$$V_{\text{neck}}(x) = \frac{1}{2}m^*\omega_{xk}^2[C_k x_k^3 + D_k x_k^4]\theta(|x| - |x_k|), \quad (4)$$

where $\theta(u) = 0$ for $u > 0$ and $\theta(u) = 1$ for $u < 0$. The four constants C_k and D_k can be expressed via two parameters as follows: $C_k = (2 - 4\epsilon_k^b)/x_k$ and $D_k = (1 - 3\epsilon_k^b)/x_k^2$, where the barrier-control parameters $\epsilon_k^b = (V_b - h_k)/V_{0k}$ are related to the height of the targeted interdot barrier (V_b , measured from the zero point of the energy scale), and $V_{0k} = m\omega_{xk}^2 x_k^2/2$.

We note that measured from the bottom of the left ($k = 1$) or right ($k = 2$) well, the interdot barrier is $V_b - \hbar\omega_k$. How we solve for the eigenvalues and eigenstates of H_{TCO} is described in Appendix A.

Motivated by the asymmetric double dot used in the GaAs device described in Ref. [15], we choose the parameters entering in the TCO Hamiltonian as follows: The left dot is elliptic with frequencies corresponding to $\hbar\omega_{x1} = 0.413\,567$ meV = 100 hGHz and $\hbar\omega_{y1} = \hbar\omega_y = 1.22$ meV = 294.9945 hGHz (1 hGHz = 4.135 67 μ eV), whereas the right dot is circular with $\hbar\omega_{x2} = \hbar\omega_{y2} = \hbar\omega_y = 1.22$ meV = 294.9945 hGHz. The left dot is located at $x_1 = -120$ nm, whereas the right dot is located at $x_2 = 75$ nm, and the interdot barrier is set to $V_b = 3.3123$ meV = 800.91 hGHz. The effective electron mass and the dielectric constant for GaAs are $m^* = 0.067m_e$ and $\kappa = 12.5$, respectively.

A. The Wigner parameter

At zero magnetic field and in the case of a single circular harmonic QD, the degree of electron localization and Wigner-molecule pattern formation can be associated with the so-called Wigner parameter [18,29],

$$R_W = Q/(\hbar\omega_0), \quad (5)$$

where Q is the Coulomb interaction strength and $\hbar\omega_0$ is the energy quantum of the harmonic potential confinement (being proportional to the one-particle kinetic energy); $Q = e^2/(\kappa l_0)$, with $l_0 = (\hbar/(m^*\omega_0))^{1/2}$ the spatial extension of the lowest state's wave function in the harmonic (parabolic) confinement.

Naturally, strong experimental signatures for the formation of Wigner molecules are not expected for values $R_W \lesssim 1$. In the double dot under consideration here, there are two different energy scales, $\hbar\omega_1 = 0.413\,567$ meV (associated with the long x dimension of the left QD) and $\hbar\omega_2 = 1.22$ meV (associated with the right circular QD). As a result, for GaAs (with $\kappa = 12.5$) one gets two different values for the Wigner parameter, namely, $R_{W,1} = 5.31$ and $R_{W,2} = 3.09$. These values suggest that a stronger Wigner molecule should form in the left QD compared to the right QD, as indeed was found by the FCI calculation described below; the essentials of the FCI method are presented in Appendix B.

We note that the earlier fabricated GaAs quantum dots had harmonic confinements associated with frequencies $\hbar\omega_0 \geq 3$ meV ($R_W < 1.97$) [34,35], which correspond to a range of smaller QD sizes that did not favor the observation of the WMs at zero magnetic fields, as can be concluded from an inspection of the earlier experimental literature [47]. In this context, the much larger anisotropic GaAs double dot of Ref. [15], as well as the findings of Ref. [14], where strong WM signatures were observed, heralds the exploration of until now untapped potentialities in the fabrication and control of quantum dot qubits.

III. CI SPECTRA AS A FUNCTION OF DETUNING

Before engaging in detailed analyses of the CI numerical results, we comment on a particular notation that will be essential in facilitating this task. Indeed, we will extensively use the three-part notation $(n_L, n_R; S)$ (with $n_L + n_R = N$)

to denote the left-well electron occupation, the right-well electron occupation, and the total spin, respectively, associated with a 3e CI wave function. In this vein, the two-part notation (n_L, n_R) will also be occasionally used

A. The big picture

Figure 1 compares the CI spectra as a function of detuning (within the same window, 1.40 meV $\leq \varepsilon \leq 2.1$ meV) for two different values of the dielectric constant, i.e., $\kappa = 1000$, which is closer to the noninteracting limit, and $\kappa = 12.5$, which is the actual value for GaAs QDs. This comparison demonstrates a dramatic modification in the spectra. Indeed, the low-energy spectrum for $\kappa = 1000$ [including the ground state, see Fig. 1(a)] is dominated by states that have the majority of electrons (two or all three electrons) residing in the deeper *right* well; such states are denoted as $(1, 2; S)$ or $(0, 3; S)$. According to the so-called branching diagram [48,49], for three electrons the allowed total spin values are $S = 1/2$ (with a multiplicity of 2) and $S = 3/2$ (with a multiplicity of 1). All five lowest-in-energy states in Fig. 1(a) have a total spin $S = 1/2$, with the $S = 3/2$ states appearing at higher energies (at the top of the plotted energy spectrum).

On the contrary, in the corresponding low-energy spectrum in the GaAs case [Fig. 1(b)], the $(2, 1; S)$ states with two electrons in the *left* well are prominent, along the $(1, 2; S)$ states with two electrons in the right well. Furthermore, states with three electrons in a given well, denoted as $(3, 0; S)$ or $(0, 3; S)$, are absent. The fact that only the six $(2, 1; S)$ and $(1, 2; S)$ states comprise the lowest-energy spectrum for the GaAs double dot is an essential feature that is a prerequisite for the implementation of the hybrid qubit, which uses [8,9,13,15,33] the four $(2, 1; 1/2)$ and $(2, 1; 3/2)$ states. As it is discussed below, this feature is the effect of the formation of Wigner molecules as a result of the strengthening of the typical Coulomb energies relative to the energy gaps in the single-particle spectrum of a confining external potential that represents a rather large-size and strongly asymmetric double dot (see the discussion on the Wigner parameter R_W in Sec. II A).

To assist the reader in the exploration of the features present in the spectra of Fig. 1, we have successively numbered the lowest six states at $\varepsilon = 1.4$ meV, starting from the ground state (no. 1) and moving upwards to the first five excited ones. Apart from the immediate neighborhood of an avoided crossing, in both spectra these energy curves are straight lines, and naturally we keep the same numbering for all values of the detuning in the window range used in Figs. 1(a) and 1(b).

In Fig. 1(a), there are no degeneracies, and this numbering is self-explanatory. The spectrum in Fig. 1(b) is less transparent because of quasidegeneracies between states 2 and 3, and 5 and 6, as well as the small energy gap (~ 3 hGHz) between state 1 and the quasidegenerate pair (nos. 2 and 3). We stress that states 1 and 2 have two electrons in the left well and total spin $S = 1/2$, and thus they are denoted as $(2, 1; 1/2)$, whereas state 3 has two electrons in the left well but a total spin of $S = 3/2$ [denoted as $(2, 1; 3/2)$]. On the other hand, states 4, 5 (with $S = 1/2$), and 6 (with $S = 3/2$) have two

electrons in the right well, and they are denoted as $(1, 2; S)$. A main feature of this six-state spectrum in Fig. 1(b) is that, apart from the neighborhoods of the two avoided crossings (see Sec. III B), the energy curves for states 1, 2, and 3 form one band of parallel lines, whereas the energy curves for the states 4, 5, and 6 form a second band of parallel lines, and the two bands intersect at two avoided crossings. Again, the appearance of such three-member bands, grouping together two $S = 1/2$ states and one $S = 3/2$ state, is a consequence of the formation of a 3e Wigner molecule (three localized electrons considering both wells), and this is in consonance with the findings of Ref. [43] regarding the spectrum of three electrons in single anisotropic quantum dots in variable magnetic fields.

We further stress that the dominant feature in the spectrum of Fig. 1(b) is the small energy gap between the two $S = 1/2$ states, 1 and 2, which contrasts with the large gap between the other two $S = 1/2$ states, 4 and 5, a point that will be discussed in detail in Sec. III C below.

1. Charge densities away from the avoided crossings

Further insight into the unique trends and properties of the GaAs double dot with the parameters listed in Sec. II is gained through an inspection of the CI-calculated charge densities, plotted in Fig. 1 for the ground and first five excited states and for both values $\kappa = 1000$ [see Figs. 1(c)–1(h)] and $\kappa = 12.5$ [see Figs. 1(i)–1(d)] of the dielectric constant.

To facilitate the identification and elucidation of the main trends, we display, along with the charge densities, the CI-obtained electron occupancies (red lettering) in the left and right wells of the DQD (rounded to the second decimal point). [These CI occupations are rounded further to the closest integer in order to yield the n_L 's and n_R 's ($n_L + n_R = 3$) used in the notation $(n_L, n_R; S)$ to characterize the energy curves in the spectra in Figs. 1(a) and 1(b).] Naturally, the charge densities are normalized to the total number of electrons, $N = 3$.

Inspection of the charge densities on the left (for $\kappa = 1000$, that is, for highly weakened interelectron repulsion) reveals that they conform to those expected from an independent-particle system. Indeed, in Figs. 1(c), 1(f) and 1(g), two electrons with opposite spins occupy the lowest nodeless $1s$ -type single-particle level in the right well. At the same time, the single electron in the left well can successively occupy the zero-node [Fig. 1(c)], one-node [Fig. 1(f)], and two-node [Fig. 1(g)] single-particle states in this well. The fifth excited state is a $(2,1)$ [Fig. 1(h)] state, with two electrons with opposite spins occupying the lowest nodeless single-particle level in the left well, whereas the third electron occupies the nodeless single-particle level of the right well. Finally, the second and third excited states [Figs. 1(d) and 1(e)] are $(0,3)$ states with all three electrons residing in the right well. In a circular dot, these two states would be degenerate and fully circular with angular momenta $+1$ and -1 , but here the degeneracy is lifted because of the influence of the left well and the interwell neck.

The charge densities on the right (for $\kappa = 12.5$, case of GaAs) deviate strongly from those expected from an independent-particle system. Indeed, the formation of a strong 2e WM in the left well and of a weaker 2e WM in the right well is clearly seen. For example, contrast the $(2,1)$

independent-particle density in Fig. 1(h) with the $(2,1)$ WM density in Figs. 1(i)–1(k) and the $(1,2)$ independent-particle density in Fig. 1(c) with the $(1,2)$ WM density in Figs. 1(l)–1(n). We also note the absence of states with higher than double occupancy in any of the DQD wells, unlike the findings for the case of the highly quenched interelectron interaction discussed above; such states may emerge as highly excited states for GaAs DQDs with the parameters used here (as well as in the experiments [15]) and need not be of concern for future application of such DQDs.

2. Spin structure away from the avoided crossings

The charge densities of the states 1, 2, and 3 in the three-member band for $\kappa = 12.5$ [see Figs. 1(i)–1(k)] are very similar. However, the corresponding spin structures are different, as shown explicitly below. Differences between the spin structures may be investigated with the employment of (1) spin-resolved densities and (2) spin-resolved conditional probability distributions. The concept of spin-resolved densities is self-evident. The concept of the spin-resolved CPDs is more complicated, and the full definition is provided in Appendix C. At the intuitive level, the spin-resolved CPD addresses the following question: given the specific (fixed) location \mathbf{r}_0 of an electron with a definite spin (up or down), what is the probability distribution at another location \mathbf{r} for finding another electron with a definite (up or down) spin?

As an example of the spin-structure analysis that can be achieved with the CI calculations, we analyze below the two cases of the ground state and the first excited state for $\kappa = 12.5$ (GaAs) and $\varepsilon = 1.405$ meV. Figures 2(a) and 2(b) display, respectively, the spin-up and spin-down densities for the ground state mentioned above; compare Fig. 1(i) for the total charge density. From these two spin-resolved densities, it is evident that the spin structure of this ground state conforms to the following familiar expression [8, 15, 41, 50] in the theory of three-electron qubits:

$$(|duu\rangle - |udu\rangle)/\sqrt{2}, \quad (6)$$

where u and d denote an up and down spin, respectively, with the three spins arranged in a line from left to right in three ordered sites, 1, 2, and 3.

Further confirmation for the spin structure in Eq. (6) is obtained from the spin-resolved CPDs, two examples of which are displayed in Figs. 2(c) and 2(d). Indeed, both the spin kets in Eq. (6) are compatible with a first electron with spin up being fixed at the third site. Then the first spin ket in Eq. (6) allows the presence of a spin-up electron in its second site with probability $1/4$, whereas the second spin ket allows the presence of a spin-up electron in its first site, again with equal probability $1/4$. This is clearly in agreement with the CI CPD plotted in Fig. 2(c), which exhibits two humps of similar height at sites 1 and 2. Likewise, only the second spin ket in Eq. (6) is compatible with a first electron with spin up being fixed in the first site, and this spin ket allows the presence of a spin-down electron in its second site with probability $1/4$. This again is in agreement with the CI CPD plotted in Fig. 2(d), which exhibits a single hump at site 2.

Figures 3(a) and 3(b) display the spin-up and spin-down densities for the associated first excited state; compare

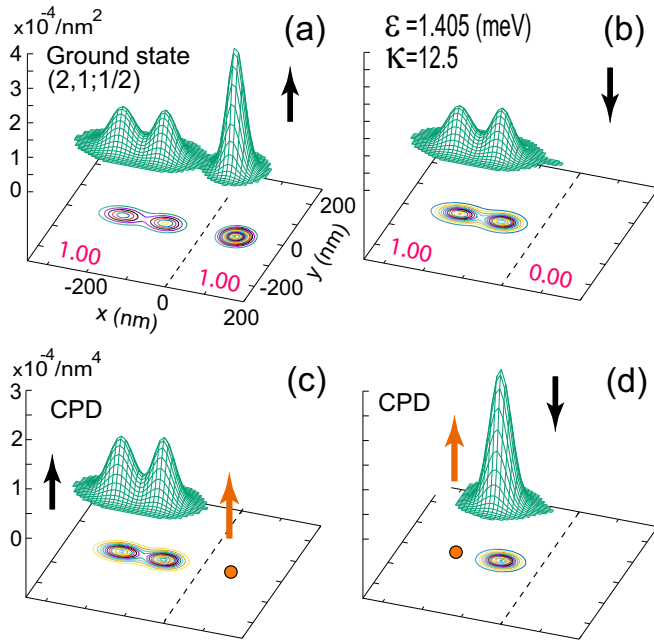


FIG. 2. The spin structure of the ground state at $\kappa = 12.5$ and $\varepsilon = 1.405$ [see Fig. 1(i) for the corresponding total charge density]. (a) The spin-up density. (b) The spin-down density. The red decimal numbers in (a) and (b) indicate the CI-calculated left and right occupancies (rounded to the second decimal point). (c, d) Examples of two of the associated spin-resolved CPDs. The red dots and arrows indicate the position and spin direction of the fixed point. The black arrows indicate the spin direction associated with the plotted surface. The spin-resolved densities integrate to the number of spin-up and spin-down electrons in (a) and (b), respectively. The scale of the vertical axes in (c) and (d) is arbitrary but the same in both cases.

Fig. 1(j) for the total charge density. From these two spin-resolved densities, one can conclude that the spin structure of this first excited state conforms to a second familiar expression [8,15,41,50] in the theory of three-electron qubits, namely,

$$(2|uud\rangle - |duu\rangle - |udu\rangle)/\sqrt{6}. \quad (7)$$

Indeed, from Eq. (7) one can derive that the expected spin-up occupancy for the most leftward and middle positions of the three spins is $5/6$ in both cases, yielding $5/3 = 1.666$ for the expected spin-up occupancy in the left dot, in agreement with the CI value of 1.66 highlighted in red in Fig. 3(a). Similarly the expected spin-up occupancy for the right dot from Eq. (7) is $1/3 = 0.333$, in agreement with the CI value of 0.34 highlighted in red in Fig. 3(a). Moreover, from Eq. (7) one can derive that the expected spin-down occupancy for the most leftward and middle positions of the three spins is $1/6$ in both cases, yielding $1/3 = 0.333$ for the expected spin-down occupancy in the left dot, in agreement with the CI value of 0.33 highlighted in red in Fig. 3(b). Finally, the expected spin-down occupancy for the right dot from Eq. (7) is $2/3 = 0.666$, in agreement with the CI value of 0.67 highlighted in red in Fig. 3(b).

As mentioned previously, further confirmation for the spin structure in Eq. (7) can be obtained from the spin-resolved CPDs, two examples of which are displayed in Figs. 3(c)

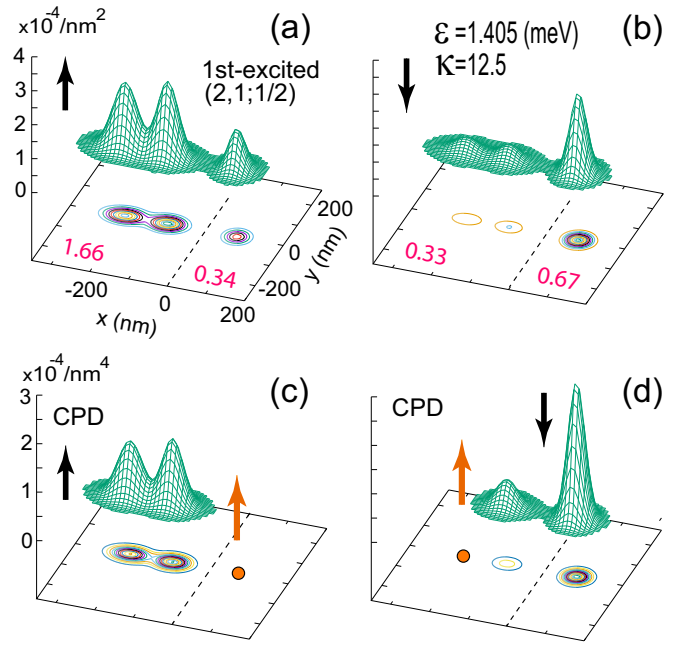


FIG. 3. The spin structure of the first excited state at $\kappa = 12.5$ and $\varepsilon = 1.405$ [see Fig. 1(j) for the corresponding total charge density]. (a) The spin-up density. (b) The spin-down density. The red decimal numbers in (a) and (b) indicate the CI-calculated left and right occupancies (rounded to the second decimal point). (c, d) Examples of two of the associated spin-resolved CPDs. The red dots and arrows indicate the position and spin direction of the fixed point. The black arrows indicate the spin direction associated with the plotted surface. The spin-resolved densities integrate to the number of spin-up and spin-down electrons in (a) and (b), respectively. The scale of the vertical axes in (c) and (d) is arbitrary but the same in both cases.

and 3(d). Indeed, only the second and third spin kets in Eq. (7) are compatible with a first electron with spin up being fixed at the third site. Then the second spin ket in Eq. (7) allows the presence of a spin-up electron in its second site with probability $1/6$, whereas the third spin ket allows the presence of a spin-up electron in its first site, again with equal probability $1/6$. This is clearly in agreement with the CI CPD plotted in Fig. 3(c), which exhibits two humps of similar height at sites 1 and 2. Likewise, only the first and third spin kets in Eq. (7) are compatible with a first electron with spin up being fixed in the first site. Then the first spin ket allows the presence of a spin-down electron in its third site with probability $2/3$, whereas the third spin ket allows the presence of a spin-down electron in its second site with probability $1/6$. This again is in agreement with the CI CPD plotted in Fig. 3(d), which exhibits two humps with relative height $1/4$ at sites 2 and 3.

We stress that the two expressions in Eqs. (6) and (7) for the spin structures of three fermions are not the most general ones. The most general [51] expression for a total spin $S = 1/2$ with a total spin projection $S_z = 1/2$ is [52]

$$\begin{aligned} & \sqrt{\frac{2}{3}} \sin \vartheta |uud\rangle + \left(\sqrt{\frac{1}{2}} \cos \vartheta - \sqrt{\frac{1}{6}} \sin \vartheta \right) |udu\rangle \\ & - \left(\sqrt{\frac{1}{2}} \cos \vartheta + \sqrt{\frac{1}{6}} \sin \vartheta \right) |duu\rangle, \end{aligned} \quad (8)$$

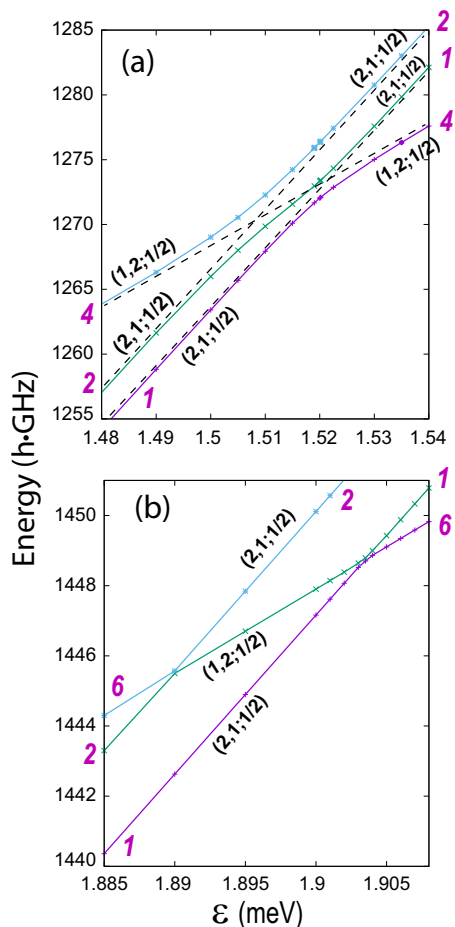


FIG. 4. Magnification of the neighborhoods of the CI avoided crossings appearing in Fig. 1(b) ($\kappa = 12.5$, case of GaAs). Only the $S = 1/2$ states, relevant to the hybrid qubit, are shown. (a) The left avoided crossing in the neighborhood of $1.49 \text{ meV} < \varepsilon < 1.54 \text{ meV}$. (b) The right avoided crossing in the neighborhood of $1.885 \text{ meV} < \varepsilon < 1.908 \text{ meV}$.

where the angle ϑ can take any value in the interval $[\pi/2, 3\pi/2]$. Equation (6) is recovered for $\vartheta = \pi$, whereas its companion orthogonal expression (7) is recovered for $\vartheta = \pi/2$. Thus it is gratifying to see that the FCI solutions, analyzed with the CPDs that are associated with the hybrid-qubit device of Ref. [15], do not deviate from the spin structures invoked in building the theoretical models of three-electron qubits [8,41,50].

B. The avoided crossings

In Figs. 4(a) and 4(b) we display magnifications of the neighborhoods of the left and right CI avoided crossings, respectively, appearing in the spectrum of the GaAs double dot [Fig. 1(b)]. Only the $S = 1/2$ states are shown, because the $S = 3/2$ states are not relevant for the workings of the hybrid qubit [8,15,41,50].

The left avoided crossing (situated in the neighborhood of $1.49 \text{ meV} < \varepsilon < 1.54 \text{ meV}$) is formed through the interaction of the three curves 1, 2, and 4 [we keep the same numbering of curves here as in Fig. 1(b)]. On the other hand,

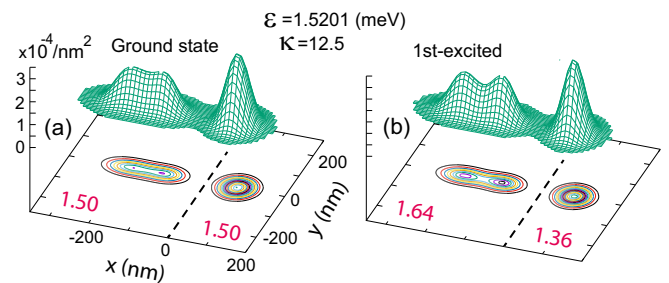


FIG. 5. Examples of charge densities at the left avoided crossing of the spectrum in Fig. 1(b), namely, at $\varepsilon = 1.5201$ and $\kappa = 12.5$. (a) The ground state. (b) The first excited state. Both states have a total spin $S = 1/2$. The red decimal numbers indicate the left-right electron occupancies according to the CI calculation (rounded to the second decimal point).

curves 1, 2, and 6 participate in the formation of the right avoided crossing in the neighborhood of $1.885 \text{ meV} < \varepsilon < 1.908 \text{ meV}$. We note that according to the FCI calculation, the two avoided crossings are separated by a detuning energy interval of $\sim 400 \mu\text{eV}$, which agrees with the experimentally determined value for the hybrid-qubit device in Ref. [15].

The continuous lines in both panels of Fig. 4 represent the so-called *adiabatic* paths, which the system follows for slow time variations of the detuning, or with an applied laser pulse, the system can instead follow the *diabatic* paths indicated explicitly with dashed lines in Fig. 4(a) and thus jump from one adiabatic line to another; this occurs according to the celebrated Landau-Zener-Stückelberg-Majorana [53–55] dynamical interference theory.

We further mention that the position and the asymmetric anatomy of the two avoided crossings play an essential role in the operation of the hybrid qubit. Indeed, the qubit is initialized on line no. 4 and in a $(1, 2; 1/2)$ ground-state configuration at a value of detuning far to the right of the left crossing. Then, by decreasing the magnitude of the detuning in an adiabatically evolving manner, the state of the qubit moves along the no. 4 line and is brought in the neighborhood of the left avoided crossing, where a laser pulse induces a small-gap-enabled diabatic transition to line no. 1 [a $(2, 1; 1/2)$ line]. Next by increasing the detuning value, the qubit operation cycle proceeds by moving adiabatically backwards along line 1 and through the right avoided crossing transitioning to line 6 [a $(1, 2; 1/2)$ line], where the readout can be implemented, aided by the large energy gap between the two $(1, 2; 1/2)$ states 4 and 6 [9,15].

I. Charge densities at the avoided crossings: Mixing of WM states

Inside the neighborhood of the avoided crossings, it is expected that the ground state will be a superposition of the two different wave functions $(2,1)$ (with two electrons in the left well) and $(1,2)$ (with two electrons in the right well). For $\kappa = 12.5$, this is confirmed by the CI ground-state charge density [see Fig. 5(a)] at the detuning value of $\varepsilon = 1.5201 \text{ meV}$ [middle point in the neighborhood of the left avoided crossing; see Fig. 4(a)]. Indeed, the associated left and right electron occupancies both equal 1.50, suggesting the CI ground state

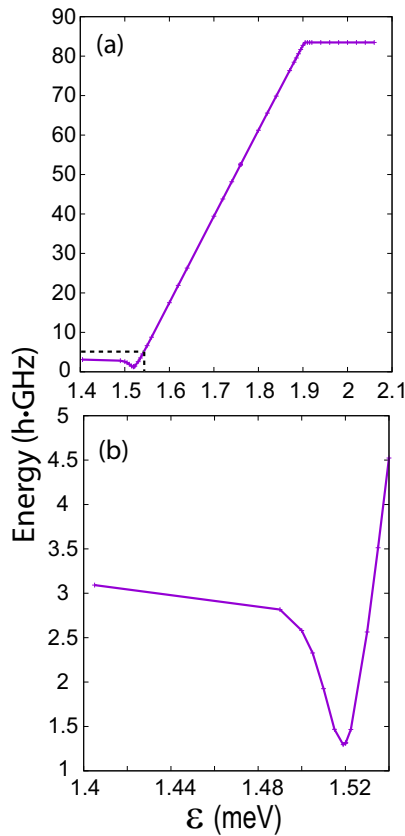


FIG. 6. The CI-calculated energy gap between ground and first excited states as a function of the detuning for $\kappa = 12.5$ (GaAs) [see the spectrum in Fig. 1(b)]. (a) In the broader range from 1.4 to 2.1 meV covering both avoided crossings. (b) In a smaller range [see the dashed-border box in (a)] covering the left avoided crossing.

is a superposition given by $(|1\rangle + |4\rangle)/\sqrt{2}$. Likewise, at the same value of $\varepsilon = 1.5201$ meV, the charge density of the first excited CI state [see Fig. 5(b)] exhibits left and right electron occupancies equal to 1.64 and 1.36, respectively, suggesting that this state is a superposition given by $0.8|1\rangle - 0.6|4\rangle$.

C. The energy gap between the ground and first excited states

To further highlight the notable specifications of the GaAs double dot considered in this paper, we display in Fig. 6 the CI-calculated energy gap between the ground and the first excited state as a function of the detuning for $\kappa = 12.5$ (GaAs) [see the spectrum in Fig. 1(b)]. Figure 6(a) displays the broader view in the detuning range from 1.4 to 2.1 meV covering both avoided crossings. In reference to the spectrum in Fig. 1(b), this energy gap involves the following states: (1) states 1 and 2 to the left of the left avoided crossing, (2) states 4 and 1 between the two avoided crossings, and (3) states 4 and 6 to the right of the right avoided crossing. Figure 6(a) highlights the overarching rise by an order of magnitude of this energy gap, from ~ 3 hGHz to ~ 83 hGHz, as the spectrum transitions from the (2,1) to the (1,2) configurations with two electrons in the left and right dots, respectively. We note that this behavior is in excellent agreement with the sharp rise

of the corresponding energy gap within a detuning range of ~ 400 μeV proposed in the experimental paper of Ref. [15] [see Fig. S5(b) therein].

Moreover, Fig. 6(b) magnifies the corresponding energy gap in a smaller range [see the dashed-border box in Fig. 6(a)] covering only the left avoided crossing. The CI-calculated curve in 6(b) exhibits remarkable overall agreement with the corresponding measured one in Fig. 1(b) of Ref. [15] [see also Fig. S5(b) therein].

D. The effective matrix Hamiltonian

In this section we extract from the CI spectra the phenomenological effective matrix Hamiltonian [9,15] that has played a central role in the experimental dynamical control of the hybrid qubit. The general form of this 4×4 matrix Hamiltonian is

$$H_M = \begin{pmatrix} c_L \tilde{\varepsilon}/2 & 0 & \delta_1 & -\delta_2 \\ 0 & c_L \tilde{\varepsilon}/2 + \Delta E_L & -\delta_3 & \delta_4 \\ \delta_1 & -\delta_3 & c_R \tilde{\varepsilon}/2 & 0 \\ -\delta_2 & \delta_4 & 0 & c_R \tilde{\varepsilon}/2 + \Delta E_R \end{pmatrix}, \quad (9)$$

where $\tilde{\varepsilon} = \varepsilon - \varepsilon_0$ denotes a renormalized interdot detuning, and the other elements of the matrix follow the notation used in Ref. [9] (see the Theory section therein).

A good fit (see Fig. 7) with the CI spectrum in Figs. 1(b) and 4 is achieved by setting $c_L = 4.4$, $\Delta E_L = 15$ μeV , $c_R = 2.7$, $\Delta E_R = 340$ μeV , $\delta_1 = 0.657$ μeV , $\delta_2 = 0.090$ μeV , $\delta_3 = 1.207$ μeV , $\delta_4 = 0.075$ μeV , and $\varepsilon_0 = 1.50$ meV.

The effective matrix Hamiltonian in Eq. (9) reflects (within the plotted window) two properties of the FCI spectrum in Fig. 1(b) that are instrumental (see, e.g., [9,56]) for the successful operation of the hybrid qubit, namely, the quasilinear dependence of H_M on the detuning ε and the quasiparallel behavior of both the two (2,1) states (states 1 and 2) and the two (1,2) states (states 4 and 6). We note a difference between Refs. [9,15] and the CI result for H_M . Namely, Refs. [9,15] assume the values $c_L = 1$ and $c_R = -1$ associated with 45° and -45° slopes of the associated lines, respectively, while the CI result produces different slopes associated with $c_L = 4.4$ and $c_R = 2.7$. We note, however, that the topology of the energy spectrum remains unaltered.

We further note that there are several derivations [8,38] of the effective Hamiltonian in Eq. (9), starting from approximate many-body Hamiltonians that include the interaction at the level of a two-site (left and right well) Hubbard-type modeling. These derivations involve several additional qualitative approximations and are not applicable in the case of strong $e - e$ correlations and Wigner-molecule formation (see Ref. [42]). Thus the reaffirmation demonstrated above regarding the overall structure of the phenomenological-in-nature effective matrix Hamiltonian [Eq. (9)], achieved here through the use of FCI-based *ab initio* calculations carried out in the regime of strong correlations and Wigner-molecule formation, is a notable result.

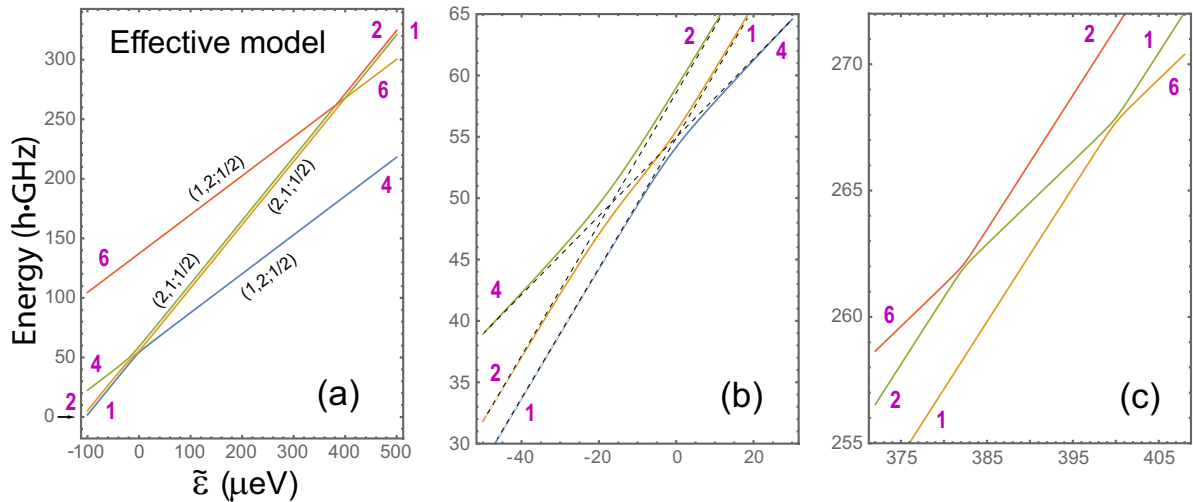


FIG. 7. The spectrum of the four hybrid-qubit states $|1\rangle$, $|2\rangle$, $|4\rangle$, and $|6\rangle$ (with $S = 1/2$) as a function of the detuning parameter $\tilde{\varepsilon} = \varepsilon - \varepsilon_0$, calculated with the effective matrix Hamiltonian in Eq. (9); $\varepsilon_0 = 1.51$ meV. (a) The full spectrum. (b) Magnification of the left avoided crossing. (c) Magnification of the right avoided crossing. For the employed values of the eight parameters c_L , δE_L , c_R , δE_R , δ_1 , δ_2 , δ_3 , and δ_4 , see the text. Note the remarkable agreement between the four-state effective spectrum here and the corresponding one of the four lowest $S = 1/2$ states in Figs. 1(b) and 4, which was generated from the FCI calculations.

IV. CI SPECTRA AS A FUNCTION OF THE DIELECTRIC CONSTANT

Further insights into the effects of the interelectron interaction can be gained by an inspection of the CI spectra as a function of the dielectric constant κ . Figure 8 portrays the spectrum of the double dot as a function of the dielectric constant κ at a detuning value of $\varepsilon = 1.50$ meV. The numbering

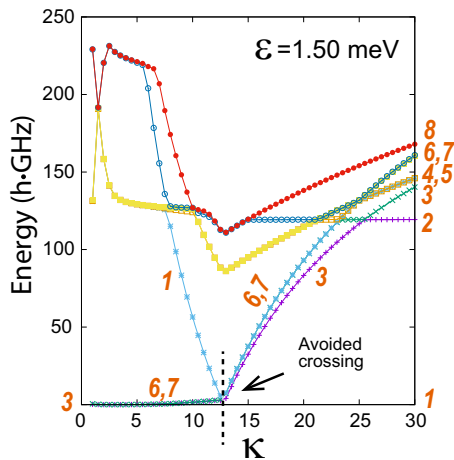


FIG. 8. Spectrum of the double dot as a function of the dielectric constant κ at a detuning value of $\varepsilon = 1.50$ meV. The numbering of the lowest eight states is performed at $\kappa = 30$, and this numbering is maintained for the whole κ range plotted. The vertical dashed line at $\kappa = 12.7$ indicates the neighborhood of the avoided crossing. Further to the left of the avoided crossing, the ground state is state no. 3 of $(2, 1; 1/2)$ character; further to the right of the avoided crossing, the ground state is state no. 1 of $(1, 2; 1/2)$ character. In the neighborhood of the avoided crossing, the ground state is a mixed state. In this plot, the ground-state energies were taken at all instances to coincide with the zero of the energy scale. For the $(n_L, n_R; S)$ designations, see Fig. 9.

of the lowest eight states is performed at $\kappa = 30$, and this numbering is maintained for the whole κ range plotted. The vertical dashed line at $\kappa = 12.7$ indicates the neighborhood of the avoided crossing. Further to the left of the avoided crossing, the ground state is state no. 3 of $(2, 1; 1/2)$ character; further to the right of the avoided crossing, the ground state is state no. 1 of $(1, 2; 1/2)$ character. In the neighborhood of the avoided crossing, the ground state is a mixed state. In this plot the ground-state energies were taken at all instances to coincide with the zero of the energy scale. The $(n_L, n_R; S)$ designations are not plotted in this figure, but they can be traced through Fig. 9, which portrays the associated charge densities.

From the charge densities in Fig. 9, one sees that at $\kappa = 30$ the three excited states 3, 7, and 7 display a 2e WM in the left dot, with the WM aligned along the x axis. With decreasing κ (increasing Coulomb repulsion), the energies of this triad of WM states exhibit a sharp drop in magnitude, and as a result they become the lowest-energy band for $\kappa < 12.7$, a fact which agrees with the findings in Sec. III A. In addition, curves 6 ($S = 3/2$) and 7 ($S = 1/2$) become quasidegenerate, and they exhibit a small energy gap (≤ 3 hGHz) from the ground state (no. 3 state), again in agreement with the findings in Sec. III A; see curves 1, 2, and 3 in Fig. 1(b).

Of interest is the fact that the ground state at $\kappa = 30$ (no. 1 state) exhibits a charge density that can be understood purely with the help of three noninteracting electrons [see Fig. 9(a)], namely, one spin-up and one spin-down electron occupying the nodeless $1s$ lowest single-particle state of the circular right well and one spin-up electron occupying the nodeless $1s_x 1s_y$ lowest single-particle state in the asymmetric left well. Naturally, as κ decreases, the intrinsic structure of the associated wave function transitions smoothly to that of a weak 2e WM in the right dot aligned along the y axis, namely, the charge density in Fig. 9(a) transitions to that portrayed in Fig. 1(l).

Of interest also are the intrinsic structures (at $\kappa = 30$) of the remaining four excited states, 2, 4, 5, and 8; they are

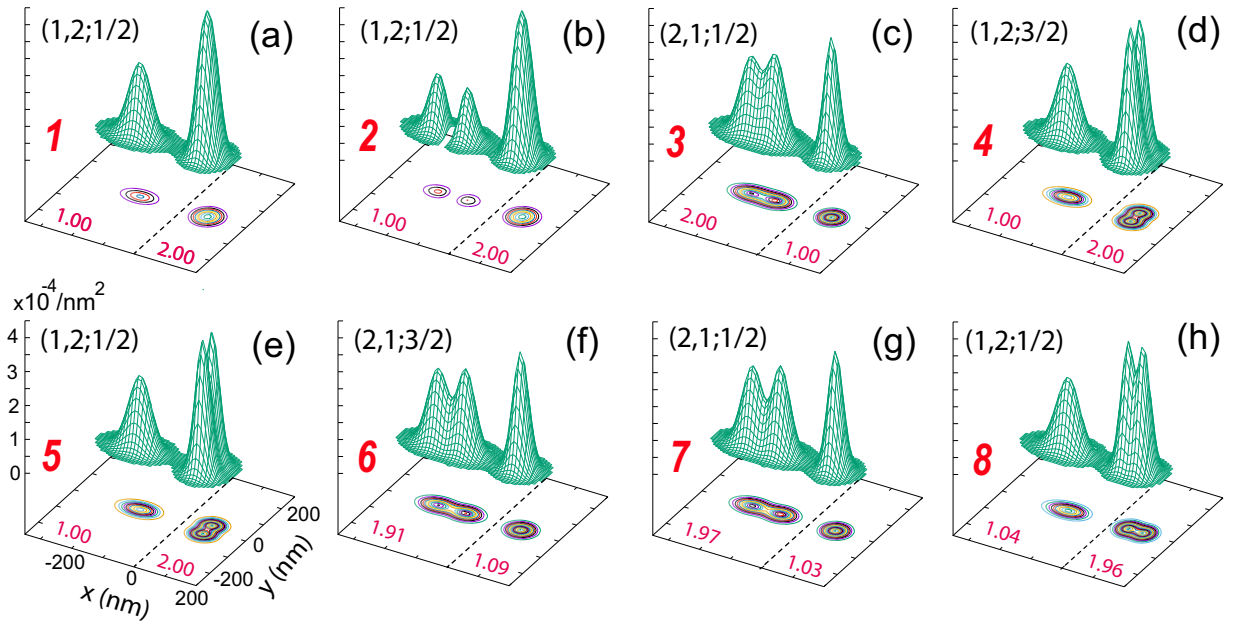


FIG. 9. Charge densities for the lowest eight states of the double quantum dot at $\kappa = 30$ and $\varepsilon = 1.50$ meV. The numbering of states is according to Fig. 8. The red decimal numbers indicate the left-right electron occupancies according to the CI calculations (rounded to the second decimal point). For a detailed description, see the text.

a testament to the variety and complexity of the 3e-DQD system. Indeed, from Fig. 9(b) one sees that excited state 2 is a noninteracting 3e state similar to state 1 but with the single spin-up electron in the left well promoted to the one-node $1p_x 1s_y$ single-particle state. On the other hand, the charge densities in Figs. 9(d) and 9(e) demonstrate that both states 4 and 5 exhibit a 2e WM in the right well with the WM aligned along the y axis. Finally, the charge density in Fig. 9(h) reveals the formation of a 2e WM in the right well but with the WM aligned along the x axis.

V. SUMMARY

We present extensive FCI numerical results that address both the energetics and the intrinsic structure of the many-body wave functions through the calculation of charge and spin-resolved densities as well as spin-resolved conditional probability distributions (spin-resolved two-body correlation functions). Going beyond the two-particle WMs studied with CI treatments in a single dot [14–17], this paper advances and enables microscopic investigations of key features appearing in the low-energy spectrum as a function of detuning of actual experimentally fabricated GaAs three-electron asymmetric HDQD qubits. These features include the strong suppression of level gaps compared to the noninteracting-electron case and the appearance of a pair of avoided crossings between triad of levels corresponding to different electron occupancies in the left and right wells. Treating the HDQD as an integral unit, we further showed in depth that these features arise from the emergence of WMs. Away from the avoided crossings, it was found that the WMs can be associated with molecular configurations centered in the individual wells. In the neighborhood of the avoided crossings, the WMs interact and form more complex resonating structures.

Earlier experimental observations had suggested that the qubit's spectral features could be codified using simple phenomenological effective matrix Hamiltonians [see, e.g., Eq. (9)]. Our double-dot extensive calculations, encompassing both energetic and structural aspects, enabled tracing of the microscopic origins of such phenomenological treatments. This phenomenology has been identified here to emerge from the complex nature of the many-body problem encountered due to the strong e-e correlations, leading to electron localization and formation of Wigner molecules.

Previous tentative derivations [8,38] of matrix Hamiltonians [of a similar structure as in Eq. (9)], starting from approximate two-site Hubbard-type modeling, involve qualitative approximations and are not applicable in the case of WM formation. Consequently, the present CI-based derivation of the effective matrix Hamiltonian in Eq. (9), achieved here via analysis using the results of FCI calculations that account fully for strong-correlation effects within each well and WM formation, is an unexpected auspicious result.

Our multidot FCI method can be expanded to incorporate the valley degree of freedom as an isospin in full analogy with the usual spin. Such an expansion will enable the acquisition of numerical results complete with full spin-isospin assignments that will reveal the underlying $SU(4) \supset SU(2) \times SU(2)$ group-chain organization of the spectra of Si double-quantum-dot qubits. This valleytronic CI [57] will be a most effective tool for analyzing the spectra of qubits and for providing effective matrix Hamiltonians that differentiate between cases when the first excited state belongs to the same or different valleys as a result of the competition [14,16] between the valley gap and strong $e-e$ interactions. In this respect, we note the case of a 5e-HDQD Si/SiGe qubit where more complex spectra, requiring an $n \times n$ matrix with $n > 4$, have been recently experimentally discovered [58]. An application of the valleytronic CI to two-qubit gates appears to be

feasible [57] in the near future, based on our estimates of the size of the required Hilbert spaces for an ensemble of $N \leq 6$ electrons confined in two interacting DQDs. Finally, beyond the GaAs-based devices, our method can be directly applied to similar devices built from other one-band materials, like holes in germanium [59,60] or silicon [17] qubits.

ACKNOWLEDGMENTS

This work has been supported by a grant from the Air Force Office of Scientific Research (AFOSR) under Award No. FA9550-21-1-0198. Calculations were carried out at the GATECH Center for Computational Materials Science.

APPENDIX A: SOLVING THE TWO-CENTER-OSCILLATOR EIGENVALUE PROBLEM

For a given interwell separation d , the single-particle levels of H_{TCO} [Eq. (3)] are obtained by numerical diagonalization in a basis consisting of the eigenstates of the auxiliary Hamiltonian:

$$H_0 = \frac{\mathbf{p}^2}{2m^*} + \frac{1}{2}m^*\omega_y^2 y^2 + \frac{1}{2}m^*\omega_{xk}^2 x_k^2 + h_k. \quad (\text{A1})$$

The eigenvalue problem associated with the auxiliary Hamiltonian [Eq. (A1)] is separable in the x and y variables, i.e., the wave functions are written as

$$\varphi_i(x, y) = X_\mu(x)Y_n(y), \quad (\text{A2})$$

with $i \equiv \{\mu, n\}$, $i = 1, 2, \dots, K$, and K specifies the size of the single-particle basis.

The $Y_n(y)$ are the eigenfunctions of a one-dimensional oscillator, and the $X_\mu(x < 0)$ or $X_\mu(x > 0)$ can be expressed through the parabolic cylinder functions $U[\gamma_k, (-1)^k \xi_k]$, where $\xi_k = x'_k \sqrt{2m^* \omega_{xk} / \hbar}$, $\gamma_k = (-E_x + h_k) / (\hbar \omega_{xk})$, and $E_x = (\mu + 0.5)\hbar \omega_{x1} + h_1$ denotes the x eigenvalues. The matching conditions at $x = 0$ for the left and right domains yield the x eigenvalues and the eigenfunctions $X_\mu(x)$. The n indices are integer. The number of μ indices is finite; they are in general real numbers.

APPENDIX B: THE CI METHOD AS ADAPTED TO THE DOUBLE-DOT CASE

As mentioned previously, we use the method of configuration interaction for determining the solution of the many-body problem specified by the Hamiltonian (1). In the CI method, one writes the many-body wave function $\Phi_N^{\text{CI}}(\mathbf{r}_1, \mathbf{r}_2, \dots, \mathbf{r}_N)$ as a linear superposition of Slater determinants $\Psi^N(\mathbf{r}_1, \mathbf{r}_2, \dots, \mathbf{r}_N)$ that span the many-body Hilbert space and are constructed out of the single-particle *spin orbitals*:

$$\chi_j(x, y) = \varphi_j(x, y)\alpha, \quad \text{if } 1 \leq j \leq K, \quad (\text{B1})$$

and

$$\chi_j(x, y) = \varphi_{j-K}(x, y)\beta, \quad \text{if } K < j \leq 2K, \quad (\text{B2})$$

where $\alpha(\beta)$ denote up (down) spins, and the spatial orbitals $\varphi_j(x, y)$ are defined in Eq. (A2). Namely,

$$\Phi_{N,q}^{\text{CI}}(\mathbf{r}_1, \dots, \mathbf{r}_N) = \sum_I C_I^q \Psi_I^N(\mathbf{r}_1, \dots, \mathbf{r}_N), \quad (\text{B3})$$

where

$$\Psi_I^N = \frac{1}{\sqrt{N!}} \begin{vmatrix} \chi_{j_1}(\mathbf{r}_1) & \dots & \chi_{j_N}(\mathbf{r}_1) \\ \vdots & \ddots & \vdots \\ \chi_{j_1}(\mathbf{r}_N) & \dots & \chi_{j_N}(\mathbf{r}_N) \end{vmatrix}, \quad (\text{B4})$$

and the master index I counts [61] the number of arrangements $\{j_1, j_2, \dots, j_N\}$ under the restriction that $1 \leq j_1 < j_2 < \dots < j_N \leq 2K$. Of course, $q = 1, 2, \dots$ counts the excitation spectrum, with $q = 1$ corresponding to the ground state.

The many-body Schrödinger equation,

$$\mathcal{H}\Phi_{N,q}^{\text{CI}} = E_{N,q}^{\text{CI}}\Phi_{N,q}^{\text{CI}}, \quad (\text{B5})$$

transforms into a matrix diagonalization problem, which yields the coefficients C_I^q and the eigenenergies $E_{N,q}^{\text{CI}}$. Because the resulting matrix is sparse, we implement its numerical diagonalization employing the well-known ARPACK solver [62]. Convergence of the many-body solutions is guaranteed by using a large enough value for the dimension K of the single-particle basis; see Appendix A. The attribute “full” is usually used for such well-converged CI solutions, which naturally contain all possible $np - nh$ basis Slater determinants.

The matrix elements $\langle \Psi_N^j | \mathcal{H} | \Psi_N^l \rangle$ between the basis determinants [see Eq. (B4)] are calculated using the Slater rules [44,63]. Naturally, an important ingredient in this respect are the matrix elements of the two-body interaction,

$$\int_{-\infty}^{\infty} \int_{-\infty}^{\infty} d\mathbf{r}_1 d\mathbf{r}_2 \varphi_i^*(\mathbf{r}_1) \varphi_j^*(\mathbf{r}_2) V(\mathbf{r}_1, \mathbf{r}_2) \varphi_k(\mathbf{r}_1) \varphi_l(\mathbf{r}_2), \quad (\text{B6})$$

in the basis formed out of the single-particle spatial orbitals $\varphi_i(\mathbf{r})$, $i = 1, 2, \dots, K$ [Eq. (A2)]. In our approach these matrix elements are determined numerically and stored separately.

The Slater determinants Ψ_I^N [see Eq. (B4)] conserve the third projection S_z but not the square $\hat{\mathbf{S}}^2$ of the total spin. However, because $\hat{\mathbf{S}}^2$ commutes with the many-body Hamiltonian, the CI solutions are automatically eigenstates of $\hat{\mathbf{S}}^2$ with eigenvalues $S(S+1)$. After diagonalization, these eigenvalues are determined by applying $\hat{\mathbf{S}}^2$ onto $\Phi_{N,q}^{\text{CI}}$ and using the relation [48]

$$\hat{\mathbf{S}}^2 \Psi_I^N = \left[(N_\alpha - N_\beta)^2 / 4 + N / 2 + \sum_{i < j} \varpi_{ij} \right] \Psi_I^N, \quad (\text{B7})$$

where the operator ϖ_{ij} interchanges the spins of fermions i and j provided that these spins are different; N_α and N_β denote the number of spin-up and spin-down fermions, respectively.

APPENDIX C: SINGLE-PARTICLE DENSITIES AND CONDITIONAL PROBABILITY DISTRIBUTIONS FROM CI WAVE FUNCTIONS

The single-particle density (charge density) is the expectation value of the one-body operator

$$\rho(\mathbf{r}) = \langle \Phi_N^{\text{CI}} | \sum_{i=1}^N \delta(\mathbf{r} - \mathbf{r}_i) | \Phi_N^{\text{CI}} \rangle, \quad (\text{C1})$$

where, as previously, Φ_N^{CI} denotes the many-body (multideterminantal) CI wave function (henceforth, we will drop the q subscript). For the spin-resolved densities, the expression above is modified as follows:

$$\rho_{\sigma}(\mathbf{r}) = \langle \Phi_N^{\text{CI}} | \sum_{i=1}^N \delta(\mathbf{r} - \mathbf{r}_i) \delta_{\sigma\sigma_i} | \Phi_N^{\text{CI}} \rangle, \quad (\text{C2})$$

where σ denotes either an up or a down spin.

Naturally, several distinct spin structures can correspond to the same charge density. The spin structure associated with a specific CI wave function can be determined uniquely with the help of the spin-resolved densities in conjunction with the many-body spin-resolved CPDs.

The spin-resolved CPDs (referred to also as spin-resolved two-point anisotropic correlation functions) yield the conditional probability distribution of finding another fermion with up (or down) spin σ at a position \mathbf{r} , assuming that a given fermion with up (or down) spin σ_0 is fixed at \mathbf{r}_0 . In detail, a spin-resolved CPD is defined as

$$P_{\sigma\sigma_0}(\mathbf{r}, \mathbf{r}_0) = \langle \Phi_N^{\text{CI}} | \sum_{i \neq j} \delta(\mathbf{r} - \mathbf{r}_i) \delta(\mathbf{r}_0 - \mathbf{r}_j) \delta_{\sigma\sigma_i} \delta_{\sigma_0\sigma_j} | \Phi_N^{\text{CI}} \rangle. \quad (\text{C3})$$

-
- [1] R. Hanson, L. P. Kouwenhoven, J. R. Petta, S. Tarucha, and L. M. K. Vandersypen, Spins in few-electron quantum dots, *Rev. Mod. Phys.* **79**, 1217 (2007).
- [2] F. A. Zwanenburg, A. S. Dzurak, A. Morello, M. Y. Simmons, L. C. L. Hollenberg, G. Klimeck, S. Rogge, S. N. Coppersmith, and M. A. Eriksson, Silicon quantum electronics, *Rev. Mod. Phys.* **85**, 961 (2013).
- [3] C. Barthel, M. Kjørgård, J. Medford, M. Stopa, C. M. Marcus, M. P. Hanson, and A. C. Gossard, Fast sensing of double-dot charge arrangement and spin state with a radio-frequency sensor quantum dot, *Phys. Rev. B* **81**, 161308(R) (2010).
- [4] A. Morello, J. J. Pla, F. A. Zwanenburg, K. W. Chan, K. Y. Tan, H. Huebl, M. Möttönen, C. D. Nugroho, C. Yang, J. A. van Donkelaar, A. D. C. Alves, D. N. Jamieson, C. C. Escott, L. C. L. Hollenberg, R. G. Clark, and A. S. Dzurak, Single-shot readout of an electron spin in silicon, *Nature (London)* **467**, 687 (2010).
- [5] L. A. Orona, J. M. Nichol, S. P. Harvey, C. G. L. Böttcher, S. Fallahi, G. C. Gardner, M. J. Manfra, and A. Yacoby, Readout of singlet-triplet qubits at large magnetic field gradients, *Phys. Rev. B* **98**, 125404 (2018).
- [6] J. Medford, J. Beil, J. M. Taylor, S. D. Bartlett, A. C. Doherty, E. I. Rashba, D. P. DiVincenzo, H. Lu, A. C. Gossard, and C. M. Marcus, Self-consistent measurement and state tomography of an exchange-only spin qubit, *Nat. Nanotechnol.* **8**, 654 (2013).
- [7] A. R. Mills, C. R. Guinn, M. J. Gullans, A. J. Sigillito, M. M. Feldman, E. Nielsen, and J. R. Petta, Two-qubit silicon quantum processor with operation fidelity exceeding 99%, *Sci. Adv.* **8**, eabn5130 (2022).
- [8] Z. Shi, C. B. Simmons, J. R. Prance, J. K. Gamble, T. S. Koh, Y.-P. Shim, X. Hu, D. E. Savage, M. G. Lagally, M. A. Eriksson, M. Friesen, and S. N. Coppersmith, Fast Hybrid Silicon Double-Quantum-Dot Qubit, *Phys. Rev. Lett.* **108**, 140503 (2012).
- [9] Z. Shi, C. B. Simmons, D. R. Ward, J. R. Prance, X. Wu, T. S. Koh, J. K. Gamble, D. E. Savage, M. G. Lagally, M. Friesen, S. N. Coppersmith, and M. A. Eriksson, Fast coherent manipulation of three-electron states in a double quantum dot, *Nat. Commun.* **5**, 3020 (2014).
- [10] D. Kim, D. R. Ward, C. B. Simmons, D. E. Savage, M. G. Lagally, M. Friesen, S. N. Coppersmith, and M. A. Eriksson, High-fidelity resonant gating of a silicon-based quantum dot hybrid qubit, *npj Quantum Inf.* **1**, 15004 (2015).
- [11] G. Cao, H.-O. Li, G.-D. Yu, B.-C. Wang, B.-B. Chen, X.-X. Song, M. Xiao, G.-C. Guo, H.-W. Jiang, X. Hu, and G.-P. Guo, Tunable Hybrid Qubit in a GaAs Double Quantum Dot, *Phys. Rev. Lett.* **116**, 086801 (2016).
- [12] B. Thorgrimsson, D. Kim, Y.-C. Yang, L. W. Smith, C. B. Simmons, D. R. Ward, R. H. Foote, J. Corrigan, D. E. Savage, M. G. Lagally, M. Friesen, S. N. Coppersmith, and M. A. Eriksson, Extending the coherence of a quantum dot hybrid qubit, *npj Quantum Inf.* **3**, 32 (2017).
- [13] B.-B. Chen, B.-C. Wang, G. Cao, H.-O. Li, M. Xiao, G.-C. Guo, H.-W. Jiang, X. Hu, and G.-P. Guo, Spin blockade and coherent dynamics of high-spin states in a three-electron double quantum dot, *Phys. Rev. B* **95**, 035408 (2017).
- [14] J. Corrigan, J. P. Dodson, H. E. Ercan, J. C. Abadillo-Uriel, B. Thorgrimsson, T. J. Knapp, N. Holman, T. McJunkin, S. F. Neyens, E. R. MacQuarrie, R. H. Foote, L. F. Edge, M. Friesen, S. N. Coppersmith, and M. A. Eriksson, Coherent Control and Spectroscopy of a Semiconductor Quantum Dot Wigner Molecule, *Phys. Rev. Lett.* **127**, 127701 (2021).
- [15] W. Jang, M.-K. Cho, H. Jang, J. Kim, J. Park, G. Kim, B. Kang, H. Jung, V. Umansky, and D. Kim, Single-shot readout of a driven hybrid qubit in a GaAs double quantum dot, *Nano Lett.* **21**, 4999 (2021).
- [16] H. E. Ercan, S. N. Coppersmith, and M. Friesen, Strong electron-electron interactions in Si/SiGe quantum dots, *Phys. Rev. B* **104**, 235302 (2021).
- [17] J. C. Abadillo-Uriel, B. Martinez, M. Filippone, and Y.-M. Niquet, Two-body Wigner molecularization in asymmetric quantum dot spin qubits, *Phys. Rev. B* **104**, 195305 (2021).
- [18] C. Yannouleas and U. Landman, Spontaneous Symmetry Breaking in Single and Molecular Quantum Dots, *Phys. Rev. Lett.* **82**, 5325 (1999); **85**, 2220(E) (2000).
- [19] R. Egger, W. Häusler, C. H. Mak, and H. Grabert, Crossover from Fermi Liquid to Wigner Molecule Behavior in Quantum Dots, *Phys. Rev. Lett.* **82**, 3320 (1999); **83**, 462(E) (1999).
- [20] C. Yannouleas and U. Landman, Formation and control of electron molecules in artificial atoms: Impurity and magnetic-field effects, *Phys. Rev. B* **61**, 15895 (2000).

- [21] C. Yannouleas and U. Landman, Collective and Independent-Particle Motion in Two-Electron Artificial Atoms, *Phys. Rev. Lett.* **85**, 1726 (2000).
- [22] A. V. Filinov, M. Bonitz, and Y. E. Lozovik, Wigner Crystallization in Mesoscopic 2D Electron Systems, *Phys. Rev. Lett.* **86**, 3851 (2001).
- [23] C. Yannouleas and U. Landman, Magnetic-field manipulation of chemical bonding in artificial molecules, *Int. J. Quantum Chem.* **90**, 699 (2002); Strongly correlated wavefunctions for artificial atoms and molecules, *J. Phys.: Condens. Matter* **14**, L591 (2002).
- [24] S. A. Mikhailov, Quantum-dot lithium in zero magnetic field: Electronic properties, thermodynamics, and Fermi liquid–Wigner solid crossover in the ground state, *Phys. Rev. B* **65**, 115312 (2002).
- [25] M. B. Tavernier, E. Anisimovas, F. M. Peeters, B. Szafran, J. Adamowski, and S. Bednarek, Four-electron quantum dot in a magnetic field, *Phys. Rev. B* **68**, 205305 (2003).
- [26] O. Ciftja and M. G. Faruk, Two-dimensional quantum-dot helium in a magnetic field: Variational theory, *Phys. Rev. B* **72**, 205334 (2005).
- [27] C. Ellenberger, T. Ihn, C. Yannouleas, U. Landman, K. Ensslin, D. Driscoll, and A. C. Gossard, Excitation Spectrum of Two Correlated Electrons in a Lateral Quantum Dot with Negligible Zeeman Splitting, *Phys. Rev. Lett.* **96**, 126806 (2006).
- [28] T. Ihn, C. Ellenberger, K. Ensslin, C. Yannouleas, U. Landman, D. C. Driscoll, and A. C. Gossard, Quantum dots based on parabolic quantum wells: Importance of electronic correlations, *Int. J. Mod. Phys. B* **21**, 1316 (2007).
- [29] C. Yannouleas and U. Landman, Symmetry breaking and quantum correlations in finite systems: Studies of quantum dots and ultracold Bose gases and related nuclear and chemical methods, *Rep. Prog. Phys.* **70**, 2067 (2007).
- [30] L. O. Baksmaty, C. Yannouleas, and U. Landman, Nonuniversal Transmission Phase Lapses through a Quantum Dot: An Exact Diagonalization of the Many-Body Transport Problem, *Phys. Rev. Lett.* **101**, 136803 (2008).
- [31] S. Kalliakos, M. Rontani, V. Pellegrini, C. P. García, A. Pinczuk, G. Goldoni, E. Molinari, L. N. Pfeiffer, and K. W. West, A molecular state of correlated electrons in a quantum dot, *Nat. Phys.* **4**, 467 (2008).
- [32] E. Wigner, On the interaction of electrons in metals, *Phys. Rev.* **46**, 1002 (1934).
- [33] D. Kim, Z. Shi, C. B. Simmons, D. R. Ward, J. R. Prance, T. S. Koh, J. K. Gamble, D. E. Savage, M. G. Lagally, M. Friesen, S. N. Coppersmith, and M. A. Eriksson, Quantum control and process tomography of a semiconductor quantum dot hybrid qubit, *Nature (London)* **511**, 70 (2014).
- [34] M. A. Bakker, S. Mehl, T. Hiltunen, A. Harju, and D. P. DiVincenzo, Validity of the single-particle description and charge noise resilience for multielectron quantum dots, *Phys. Rev. B* **91**, 155425 (2015).
- [35] See an early review on quantum dots: L. P. Kouwenhoven, C. M. Marcus, P. L. McEuen, S. Tarucha, R. M. Westervelt, and N. S. Wingreen, Electron transport in quantum dots, in *Mesoscopic Electron Transport*, edited by L. L. Sohn, L. P. Kouwenhoven, and G. Schön, NATO ASI Series (Series E: Applied Sciences) Vol 345. (Springer, Dordrecht, 1997), pp. 105–214.
- [36] C. A. Stafford and S. Das Sarma, Collective Coulomb Blockade in an Array of Quantum Dots: A Mott-Hubbard Approach, *Phys. Rev. Lett.* **72**, 3590 (1994).
- [37] G. Burkard, D. Loss, and D. P. DiVincenzo, Coupled quantum dots as quantum gates *Phys. Rev. B* **59**, 2070 (1999).
- [38] E. Ferraro, M. De Michielis, G. Mazzeo, M. Fanciulli, and E. Prati, Effective Hamiltonian for the hybrid double quantum dot qubit, *Quantum Inf. Process.* **13**, 1155 (2014).
- [39] S. Yang, X. Wang, and S. Das Sarma, Generic Hubbard model description of semiconductor quantum-dot spin qubits, *Phys. Rev. B* **83**, 161301(R) (2011).
- [40] S. Das Sarma, X. Wang, and S. Yang, Hubbard model description of silicon spin qubits: Charge stability diagram and tunnel coupling in Si double quantum dots, *Phys. Rev. B* **83**, 235314 (2011).
- [41] M. Russ and G. Burkard, Three-electron spin qubits, *J. Phys.: Condens. Matter* **29**, 393001 (2017).
- [42] Each site in these *two-site* models [8,36–41] is associated with a given dot in the double-dot device. It is then unavoidable to use the single-particle orbital eigenstates of the separated dots (see Fig. 3 in the Supplemental Material of Ref. [8]) in order to construct an approximate many-body wave function for the double-dot qubit. This approach cannot describe the many-body wave function in the case of strong $e-e$ correlations and Wigner-molecule formation, when (due to the absence of rotational symmetry in the double dot) the electrons localize within each dot at fixed positions that can only be extracted by plotting the spin-unresolved and spin-resolved densities (see Secs. III A 1 and III A 2) as a derivative result from a full CI calculation. In the case of strong WM formation, the localized electrons (or fermionic particles in general) can be approximately described by *displaced Gaussians*, and a mapping can be established between CI densities (as well as conditional probabilities; see Appendix C for definitions) and spin eigenfunctions (see Ref. [48] and Eqs. (6) and (7)). Such a mapping was discussed in detail in Ref. [44] for four electrons in a double quantum dot and for three ultracold fermionic atoms in a double optical trap in C. Yannouleas, B. B. Brandt, and U. Landman, Ultracold few fermionic atoms in needle-shaped double wells: Spin chains and resonating spin clusters from microscopic Hamiltonians emulated via antiferromagnetic Heisenberg and $t-J$ models, *New J. Phys.* **18**, 073018 (2016). This strong-WM \leftrightarrow spin-eigenfunctions mapping implies that the strong-WM physics can be interpreted qualitatively using the limiting case (for large U/t) of the Hubbard model known as the Heisenberg model. At a minimum, however, the number of sites in such a Heisenberg modeling is N (the number of localized fermions), and even larger in the case of a resonance between the left and right potential wells; for details, see again the two references mentioned above in this footnote. Elaborating further on such a Heisenberg-model interpretation in the context of a double-dot qubit is beyond the scope of the present paper.
- [43] Y. Li, C. Yannouleas, and U. Landman, Three-electron anisotropic quantum dots in variable magnetic fields: Exact results for excitation spectra, spin structures, and entanglement, *Phys. Rev. B* **76**, 245310 (2007); **81**, 049902(E) (2010).
- [44] Y. Li, C. Yannouleas, and U. Landman, Artificial quantum-dot helium molecules: Electronic spectra, spin structures, and Heisenberg clusters, *Phys. Rev. B* **80**, 045326 (2009).

- [45] For a historical perspective of the CI method in the field of quantum chemistry, see I. Shavitt, The history and evolution of configuration interaction, *Mol. Phys.* **94**, 3 (1998).
- [46] For a detailed discussion of these two methodologies in the context of QDs, see the review article in Ref. [29].
- [47] See, e.g., L. P. Kouwenhoven, D. G. Austing, and S. Tarucha, Few-electron quantum dots, *Rep. Prog. Phys.* **64**, 701 (2001).
- [48] R. Pauncz, *The Construction of Spin Eigenfunctions: An Exercise Book* (Kluwer Academic/Plenum Publishers, New York, 2000).
- [49] See Sec. IV and Fig. 2 in Ref. [44].
- [50] D. P. DiVincenzo, D. Bacon, J. Kempe, G. Burkard, and K. B. Whaley, Universal quantum computation with the exchange interaction, *Nature (London)* **408**, 339 (2000).
- [51] The energy spectra do not depend on the total-spin projection S_z . However, the many-body wave functions and the associated spin structures do depend on S_z .
- [52] See Y. Suzuki and K. Varga, *Stochastic Variational Approach to Quantum-Mechanical Few-Body Problems* (Springer, Berlin, 1998); see also Ying Li, Ph.D. dissertation, Georgia Institute of Technology, 2009, Chap. 3.4.2, <http://hdl.handle.net/1853/28186>.
- [53] G. Cao, H. O. Li, T. Tu, L. Wang, C. Zhou, M. Xiao, G. C. Guo, H. W. Jiang, and G.-P. Guo, Ultrafast universal quantum control of a quantum-dot charge qubit using Landau-Zener-Stückelberg interference, *Nat. Commun.* **4**, 1401 (2013).
- [54] T. S. Koh, J. K. Gamble, M. Friesen, M. A. Eriksson, and S. N. Coppersmith, Pulse-Gated Quantum-Dot Hybrid Qubit, *Phys. Rev. Lett.* **109**, 250503 (2012).
- [55] H. Ribeiro, J. R. Petta, and G. Burkard, Interplay of charge and spin coherence in Landau-Zener-Stückelberg-Majorana interferometry, *Phys. Rev. B* **87**, 235318 (2013).
- [56] B.-C. Wang, G. Cao, H.-O. Li, M. Xiao, G.-C. Guo, X. Hu, H.-W. Jiang, and G.-P. Guo, Tunable Hybrid Qubit in a Triple Quantum Dot, *Phys. Rev. Appl.* **8**, 064035 (2017).
- [57] C. Yannouleas and U. Landman (unpublished).
- [58] See Sec. S5 in the Supplemental Material of Ref. [14].
- [59] N. W. Hendrickx, D. P. Franke, A. Sammak, G. Scappucci, and M. Veldhorst, Fast two-qubit logic with holes in germanium, *Nature (London)* **577**, 487 (2020).
- [60] N. W. Hendrickx, W. I. L. Lawrie, M. Russ, F. van Riggelen, S. L. de Snoo, R. N. Schouten, A. Sammak, G. Scappucci, and M. Veldhorst, A four-qubit germanium quantum processor, *Nature (London)* **591**, 580 (2021).
- [61] The question of the optimal set of expansion coefficients C_I^q (in the sense of providing the *most rapid numerical convergence*) in Eq. (B3) was answered via the introduction of the concept of natural orbitals in P.-O. Löwdin, Quantum theory of many-particle systems. I. Physical interpretations by means of density matrices, natural spin-orbitals, and convergence problems in the method of configurational interaction, *Phys. Rev.* **97**, 1474 (1955); and in P.-O. Löwdin and H. Shull, Natural orbitals in the quantum theory of two-electron systems, *ibid.* **101**, 1730 (1956). See also p. 8 in Ref. [45], and E. R. Davidson, Properties and uses of natural orbitals, *Rev. Mod. Phys.* **44**, 451 (1972). For a use of this optimal expansion in the case of two fermions confined in a double-well potential, see B. B. Brandt, C. Yannouleas, and U. Landman, Double-well ultracold-fermions computational microscopy: Wave-function anatomy of attractive-pairing and Wigner-molecule entanglement and natural orbitals, *Nano Lett.* **15**, 7105 (2015); in particular, see therein the section “Quantifying entanglement using the von Neumann entropy as a measure and the natural orbitals” and the insets in Fig. 4, where the occupations of the natural orbitals are plotted for several instances. For a similar analysis for two electrons in an elliptic quantum dot, see C. Yannouleas and U. Landman, Electron and boson clusters in confined geometries: Symmetry breaking in quantum dots and harmonic traps, *Proc. Natl. Acad. Sci. USA* **103**, 10600 (2006); Symmetry breaking and Wigner molecules in few-electron quantum dots, *Phys. Status Solidi A* **203**, 1160 (2006).
- [62] R. B. Lehoucq, D. C. Sorensen, and C. Yang, *ARPACK USERS' GUIDE: Solution of Large-Scale Eigenvalue Problems with Implicitly Restarted ARNOLDI Methods* (SIAM, Philadelphia, 1998).
- [63] A. Szabo and N. S. Ostlund, *Modern Quantum Chemistry* (McGraw-Hill, New York, 1989), Chap. 4.